Supporting Information

In-situ Surface Matrix Solidification of $FAPbI_3$ Perovskite Quantum Dots for Solar Cells with 19.37% Efficiency

Sicong Huang†, Mingxu Zhang†, Guoliang Wang, Zehong Yuan, Zhimei Sun*, and Xiaoliang Zhang*

School of Materials Science and Engineering, Beihang University, Beijing, 100191, China.

E-mail: zmsun@buaa.edu.cn; xiaoliang.zhang@buaa.edu.cn

† S. Huang and M. Zhang contributed equally to this work.

Supporting Information Contents

1. Experimental Section

Materials: All reagents were utilized as received without extra purification. Octadecene (ODE, >90% (GC)), oleic acid (OA, technical grade 90%), oleylamine (OAm, technical grade 80-90%), n-hexane (>99% (GC)), n-octane (>99% (GC)), methyl acetate (MeOAc, anhydrous 99.5%), benzoylhydrazine (BHZ, ≥98%), and lead (II) nitrate ($Pb(NO_3)_2$), ≥99.999%) were purchased from Aladdin. Iodine (I_2, 99.8%) was purchased from Beijing InnoChem Science & Technology Co., Ltd. 2-Pentanol (2-PeOH, 99%), isopropanol (IPA, 99%), chlorobenzene (CB, anhydrous, 99.8%), and tin (II) oxide (SnO_2, 15% in H_2O colloidal dispersion) were obtained from Alfa Aesar. Lead iodide (PbI_2, 99%), 2-phenylethylamine hydroiodide (PEAI, ≥99.5%), 2,2′,7,7′-tetrakis(N,N-di-p-methoxyphenylamine)-9,9′-spirobifluorene (Spiro-OMeTAD, ≥99.5%), phenyl-C61-butyric acid methyl ester (PCBM) and tris (2-(1H-pyrazol-1-yl)-4-tert-butylpyridine)-cobalt(III) tris(bis(trifluoromethylsulfonyl)imide) (FK209) were supplied by Xi'an Polymer Light Technology Corp. Toluene (TL, 99%), and chloroform (CF, 99%) were procured from Beijing Chemical Works. Acetonitrile (ACN, ≥99.9% (HPLC)), 4-tert-butylpyridine (4-TBP, 96%), lithium bis-(trifluoromethylsulfonyl)imide (Li-TFSI), and acetonitrile (anhydrous, 99.8%) were obtained from Sigma-Aldrich.

Preparation of BHZ-I_2 solution: The preparation of the BHZ-I_2 solution was based on the reaction of the BHZ and I_2 in chloroform. 25.4 mg of I_2 was added to 10 mL of chloroform to obtain the I_2 solution (0.01 M), while 27.2 mg of the BHZ was added to 5 mL of chloroform to obtain the BHZ solution (0.04 M). Next, the I_2 and BHZ solutions were mixed with the molar ratios of 1:0.5, 1:1, 1:1.5, 1:2, 1:3, 1:4, 1:5, and 1:10, with appropriate chloroform to make each BHZ-I_2 solution equal in volume. The solutions were stored in a dark environment for 12 h to fully react. All the solutions were filtered through a 0.25 μm polytetrafluoroethylene (PTFE) filter before light absorption measurement.

Preparation of BZI solution: The preparation of the BZI solution was based on the reaction of the BHZ and I_2 in the acetonitrile solvent. 7.1 mg of I_2 and 15.4 mg of BHZ (molar ratio=1:4) were dissolved in 5.625 mL acetonitrile to obtain a concentration of 4 mg/mL BZI solution. The solution was stored for 12 h and filtered through a 0.25 μm PTFE filter before use. The solution was then diluted to 1, 2, and 3 mg/mL BZI solution with appropriate acetonitrile for PQD purification.

Synthesis of PQDs: $FAPbI_3$ PQDs were synthesized according to the literature with small

modifications.[1] Briefly, 0.78 g of FAAc and 15 mL of OA were mixed in a three-neck flask at 50 ℃ for 30 min. Then, the flask was heated to 120 ℃ under N_2 atmosphere and kept for 5 min to prepare the FA-oleate (FA-OA), which was cooled to 80 ℃ and maintained at that temperature for further use. Simultaneously, in another three-neck flask, 0.688 mg of PbI_2 and 40 mL of ODE were added and heated at 120 ℃ for an hour. Subsequently, 8 mL of OA and 4 mL of OAm were injected into the flask. The mixture was then heated under vacuum until the solution became clear. Afterward, the temperature was cooled to 80 ℃ under N_2 atmosphere, and the FA-OA solution was rapidly injected into the flask. After 5-7 s, the mixture was quenched in an ice-water bath.

Purification of PQDs: The purification process was mainly divided into two steps under the ambient conditions with the humidity of ~30%. In the first step, 54 mL of 2-pentanol was added to the crude PQDs solution to remove excess species and wash off some ligands from the PQD surface. The solution was then centrifuged at 8000 rpm for 5 min, and the supernatant was discarded. The PQDs were then redispersed in toluene. In the second step, pure acetonitrile, I_2 (0.46 mg/mL in ACN), BHZ (1 mg/mL in ACN) or BZI solution was added to the PQD solution as an antisolvent (volume ratio of the antisolvent to PQD solution is 1:4). After mixing thoroughly, the solution was centrifuged at 8000 rpm for 5 min. The deposited solid was dissolved in n-hexane and centrifuged at 4000 rpm for 5 min to remove residual salts and aggregated PQDs.

Fabrication of PQDSCs: The ITO glass substrate underwent a cleaning process involving sequential ultrasonication in deionized water, acetone, and ethanol. Subsequently, the ITO substrate was subjected to the ultraviolet-ozone treatment for 20 min. The SnO_2 nanoparticle solution was prepared by diluting the SnO_2 nanoparticle solution with deionized water. The diluted SnO_2 solution (2.67%, diluted with deionized water) was then spin-coated onto the ITO substrate at a speed of 4000 rpm for 30 s. The resulting sample was sintered at 150 ℃ for 30 min under ambient conditions. Before deposition of the PQD solid film, the SnO_2 film was subjected to ultraviolet-ozone treatment for 15 min. The deposition of PQD solid film was carried out at a temperature of 15-20℃ and a relative humidity of 25-30%. The ligand solution was prepared by dissolving $Pb(NO_3)_2$ in MeOAc with sonication for ~20 min, and excess salts were removed through centrifugation at 4000 rpm for 5 min. The PQD solution was spin-coated onto the SnO_2 film at 1000 rpm for 10 s, followed by a higher speed of 2000 rpm for 20 s. Then, the PQD solid film was briefly immersed in the ligand solution for 3-5 s, followed by rinsing with MeOAc. This process was

repeated 5 times to achieve the desired thickness of the PQD solid film. The PQD solid film was then transferred to an N_2 glovebox at a temperature of 15-20℃ for hole transport layer deposition. The hole transport layer was spin-coated onto the PQD solid film at 4000 rpm for 30 s, using a solution composed of 72.3 mg of Spiro-OMeTAD, 28.8 μL of 4-tBP, 17.5 μL of bis(trifluoromethane) sulfonamide lithium salt (Li-TFSI) stock solution (520 mg/mL in ACN), and 10 μL of Co-complex (FK209) stock solution (300 mg/mL in ACN) in 1 mL chlorobenzene. Finally, the MoO_x and Ag layers were deposited onto the Spiro-OMeTAD layer through thermal evaporation.

Material Characterization: The transmission electron microscope (JSM 2100) was employed to acquire TEM images at an accelerating voltage of 200 kV. A scanning electron microscope (JEOL-7500) was employed at an accelerating voltage of 3 kV to measure SEM images. Fourier transform infrared spectroscopy spectrum was recorded using the Nicolet 6700 Fourier Transform Infrared Spectrometer in transmittance mode, and the PQD solid film was deposited on a CaF_2 glass for the measurement. Light absorption and photoluminescence spectra were measured using the Ocean MAYA2000PRO spectrometer and the Fluorolog spectrophotometer (HORIBA JOBIN YVON) with an excitation wavelength of 441 nm. The X-ray diffraction pattern was measured using Rigaku D/max2500 with Cu Ka radiation (λ = 1.54178 Å). Grazing incidence wide-angle X-ray scattering and grazing incidence small-angle X-ray scattering patterns were obtained using Xeuss 3.0 HR with Mo Ka radiation (λ = 1.54189 Å). X-ray photoelectron spectroscopy spectra were recorded with the Thermo Scientific Escalab 250Xi US equipped with a micro-focus monochromatic Al Kα X-ray source. The instrument resolution was determined to be 0.45 eV based on the Ag 3d5/2 peak. For atomic force microscopy imaging and surface roughness measurements, the Veeco/Bruker equipment with the ICON model was applied.

Photovoltaic performance measurement of PQDSCs: The current density-voltage (*J-V*) curve was measured using a Keithley 2400 digital source meter, while the AAA-class solar simulator (Enlil SS-F5-3A) provided AM1.5G illumination with a light intensity of 100 mW/cm^2. Before the *J-V* measurement, the light intensity was calibrated using a certified reference Si solar cell (Fraunhofer ISE). The measurement was performed under a nitrogen atmosphere to prevent degradation. The active area of PQDSCs was 0.04 cm^2, which was defined using a black metallic mask. The incident photon-to-electron conversion efficiency (IPCE) spectrum was recorded using the Enli Technology QE-R

system, comprising a xenon lamp (QE-LD), a Czerny-Turner monochromator (QE-M110), an optical imaging system, and a light intensity detection system (QE-M1). Before the measurement, the setup was calibrated using a certified reference silicon solar cell (SRC 2020). The photostability of PQDSCs was tested using the solar cell stability test setup (PV-S-16, Tianjin Meitong, China), which was conducted under continuous 100 mW/cm^2 illumination provided by a white LED (MT-LED-80, Tianjin Meitong, China). Transient photovoltage (TPV), transient photocurrent (TPC) and electrochemical impedance spectroscopy (EIS) of PQDSCs were recorded using the Zahner Xenium 5C-Pro electrochemical workstation.

Theoretical Calculations: First-principles calculations were performed employing the Vienna Ab initio Simulation Package (VASP).[2] The electron-ion interaction was described using the projected-augmented-wave (PAW) method, while Grimme's DFT-D3 was applied for dispersion correction. All calculations employed a plane-wave basis set with an energy cutoff of 400 eV. To model the PQD surfaces, a slab with 3×2 periodicity in the a-b plane and a 15 Å vacuum along the c-axis was utilized. The surface structure of the PQD was optimized until the forces were below 0.05 eV/Å and the energy below 1.0×10^{-5} eV. For the Brillouin zone, a Monk Horst-Pack k-point mesh of (2×2×1) was adopted. The binding energy ($E_{binding}$) was defined as $E_{binding} = E_{total} - E_{additive} - E_{surface}$, with E_{total} denoting the total energy of the system following structural optimization, while $E_{additive}$ and $E_{surface}$ correspond to the energy of the added ligand and the surface slab, respectively.[3]

2. Supplementary Figures

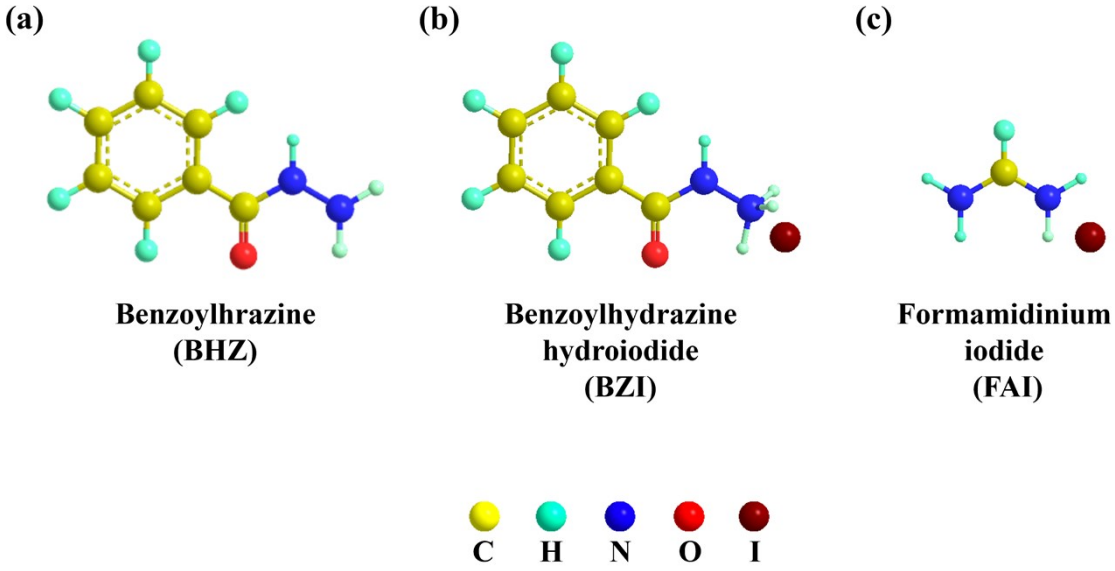

Figure S1. Molecular structure of (a) BHZ, (a) BZI, and (c) FAI.

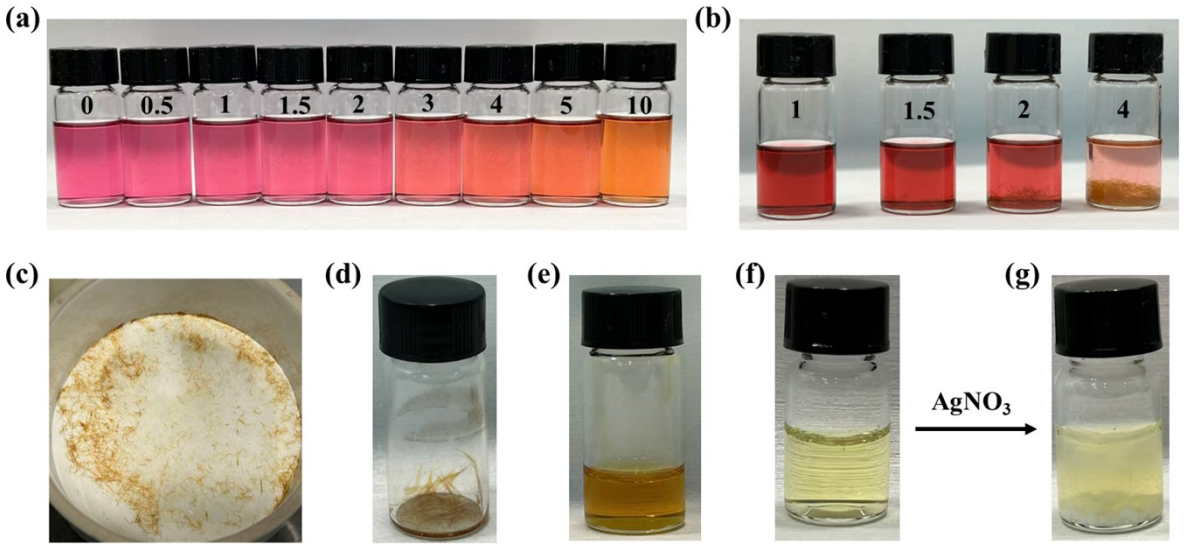

Figure S2. (a) Photographs of the mixed BHZ and I_2 with different molar ratios. (b) After 12 hours of reduction reaction, the acicular crystals (BZI) were observed in the solutions with BHZ:I_2 molar ratios of 1.5, 2 and 4, whereas these acicular crystals were hardly observed in the solution with the BHZ:I_2 molar ratio of 1. Collected acicular crystals (c) on the filter paper and (d) in a vial. The acicular crystals were dissolved in (e) DMSO and (f) H_2O. (g) Adding 50 μL $AgNO_3$ (aq) to the vial of (f), the light-yellow precipitation formed rapidly.

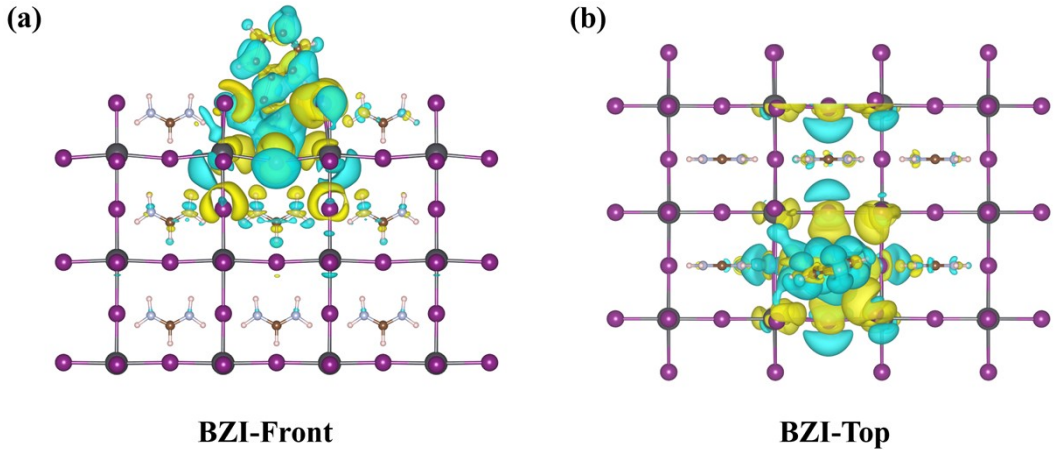

Figure S3. (a) Front and (b) top view of differential charge density maps of the BZI ligand anchored on the surface matrix of the PQD surface. The yellow electron clouds surrounding the I^- ions near the BZ^+ ligand represent charge accumulation, suggesting strong interactions between the BZ^+ ligand and I^- ions.

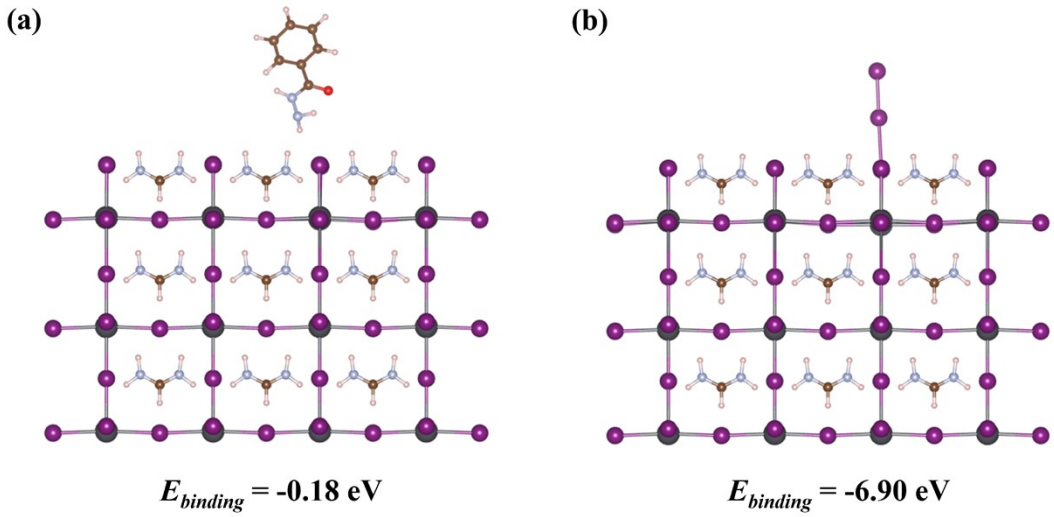

Figure S4. (a) Optimized structures of the PQD with a BHZ ligand absorbing on the surface. (b) Optimized structures of the PQD with an I_3^- ligand on the V_I on the surface matrix.

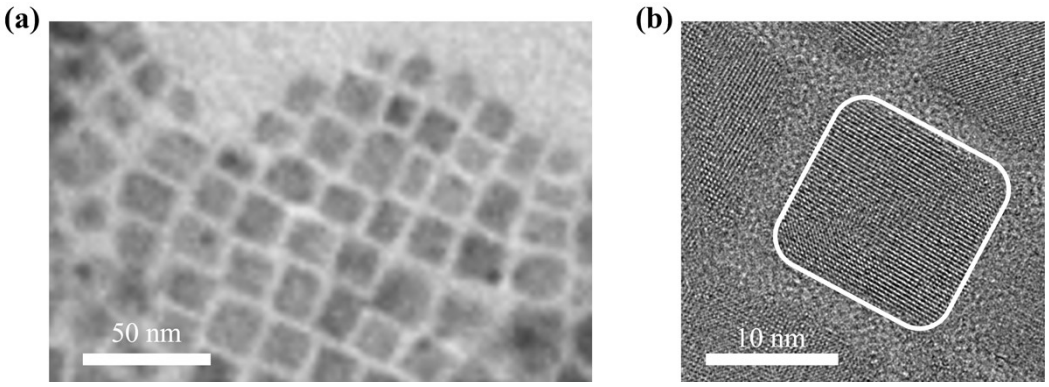

Figure S5. (a) TEM and (b) HETEM images of $FAPbI_3$ PQDs.

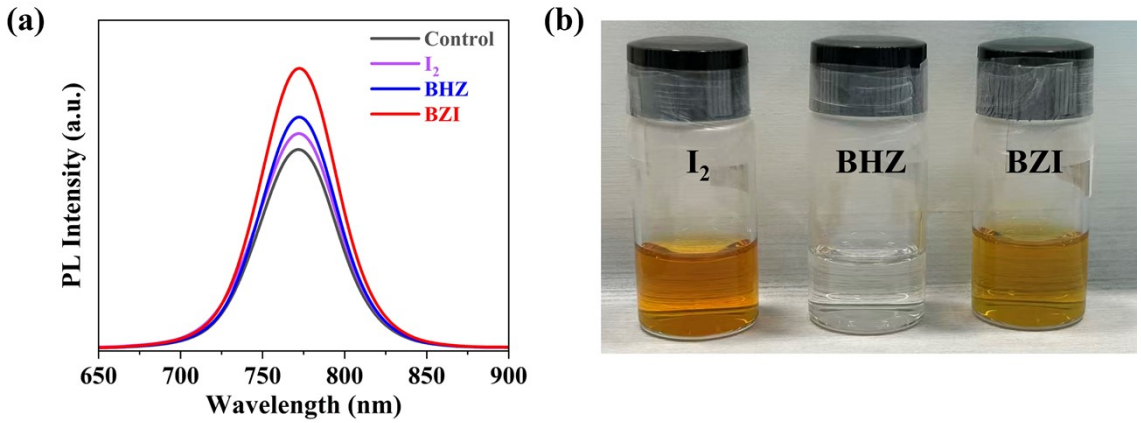

Figure S6. (a) Steady-state PL spectra of control, I_2-, BHZ-, and BZI-based PQDs. (b) Photographs of I_2, BHZ, and BZI solutions.

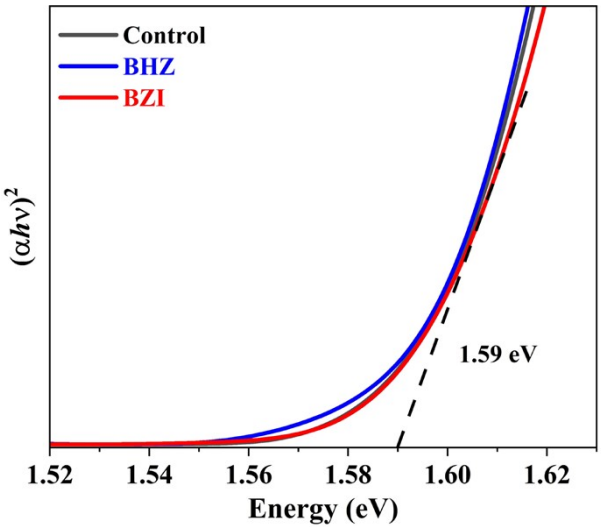

Figure S7. Tauc plots of control, BHZ-, and BZI-based PQDs.

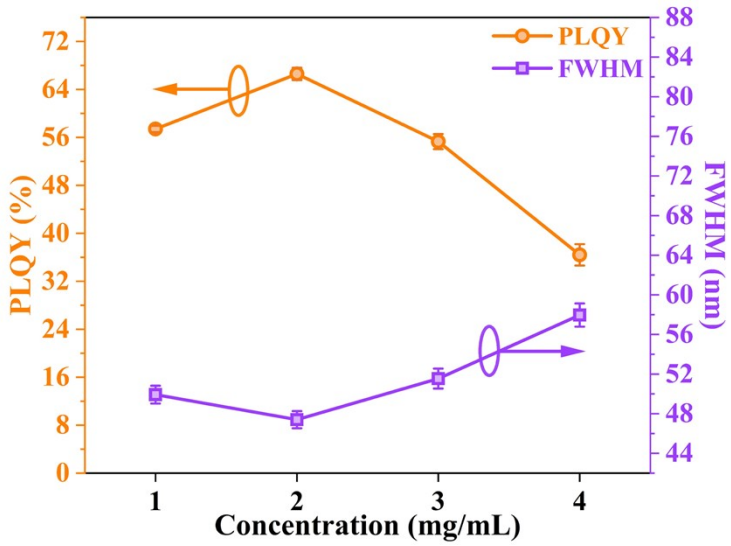

Figure S8. PLQY and FWHM of the BZI-based PQDs treated with different concentrations of the BZI ligands. The BZI solution with a concentration of 4 mg/mL was prepared by dissolving 7.1 mg of I_2 and 15.4 mg of BHZ in 5.625 mL ACN. The solution was stored for 12 h and filtered through a 0.25 μm PTFE filter before use. Then, the BZI was diluted to 1, 2, and 3 mg/mL with appropriate acetonitrile.

For each concentration, 5 independent PLQY/FWHM data of corresponding BZI-based PQDs were applied for statistics.

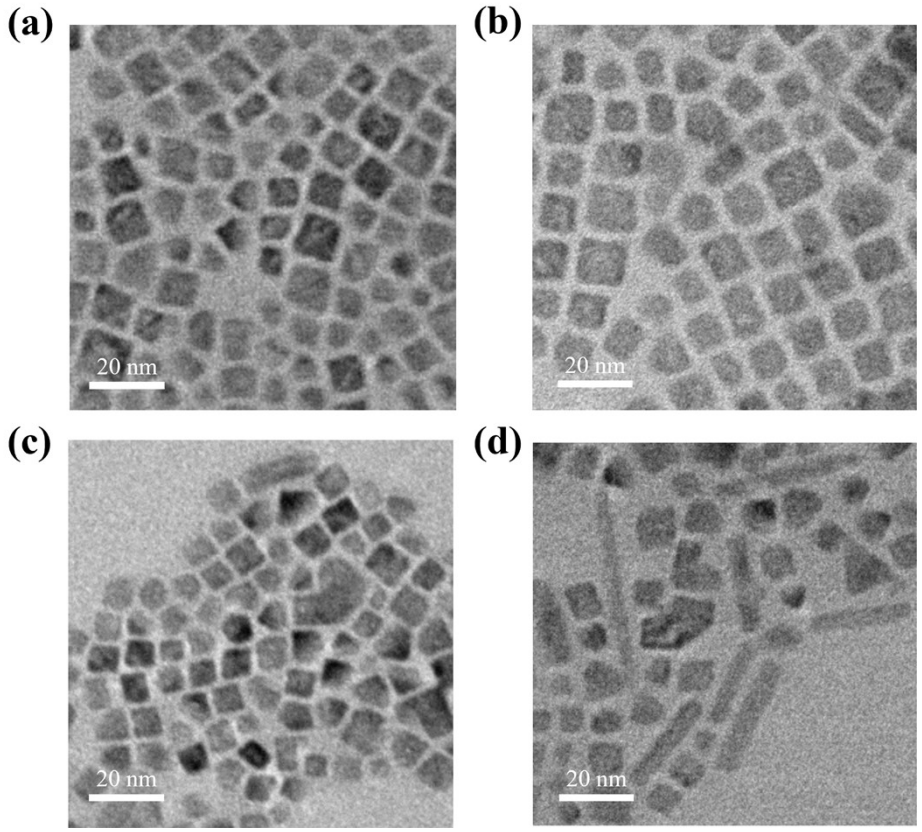

Figure S9. TEM images of the PQDs treated with (a) 1 mg/mL, (b) 2 mg/mL, (c) 3 mg/mL, and (d) 4 mg/mL of BZI solutions.

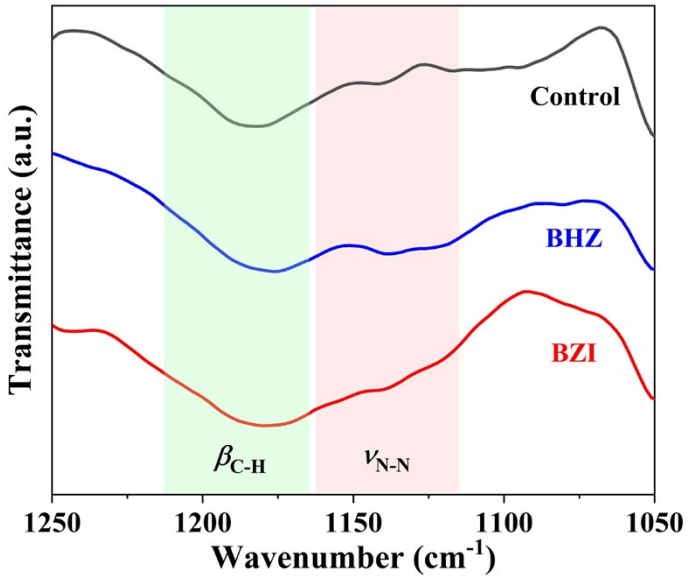

Figure S10. Amplified FTIR spectra in the 1050-1250 cm^{-1} region of control, BHZ-, and BZI-based PQDs.

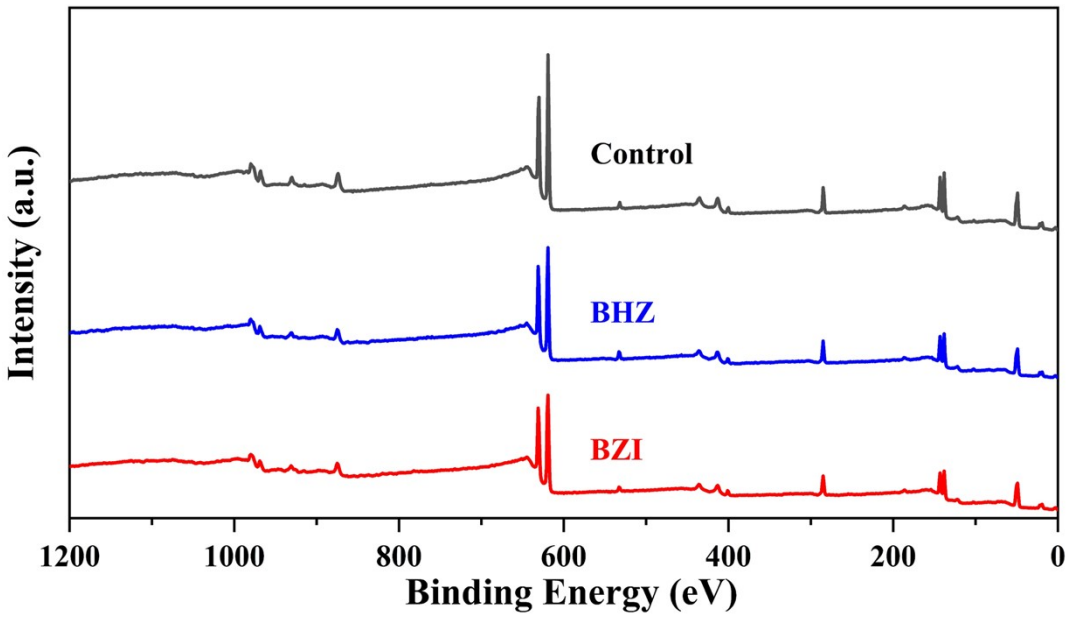

Figure S11. The overview XPS spectra of control, BHZ-, and BZI-based PQDs.

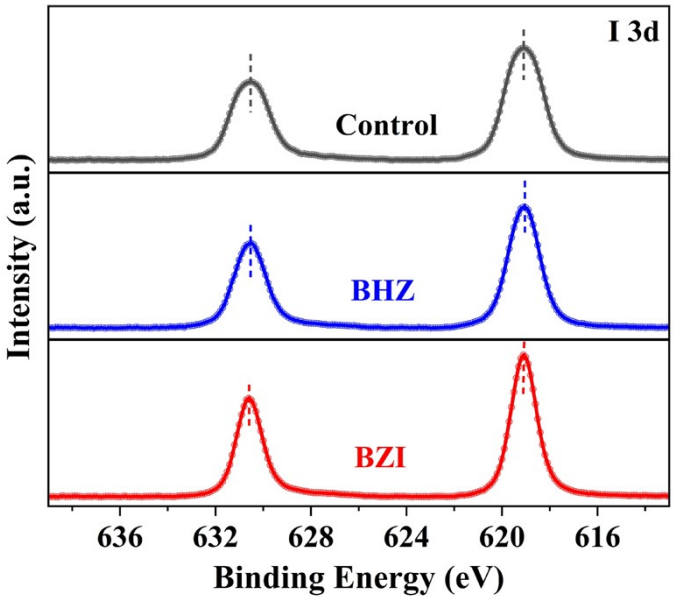

Figure S12. I 3d core-level XPS spectra of control, BHZ-, and BZI-based PQDs.

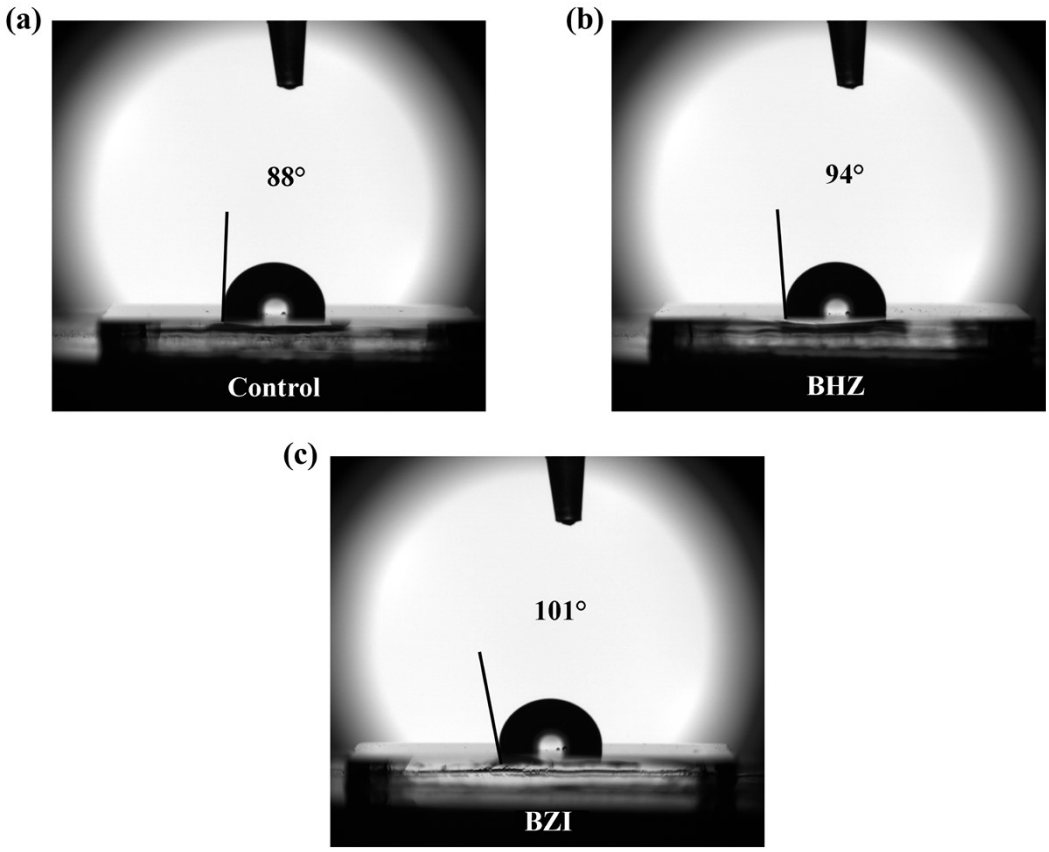

Figure S13. The water contact angles of (a) control, (b) BHZ-, and (c) BZI-based PQD solid films.

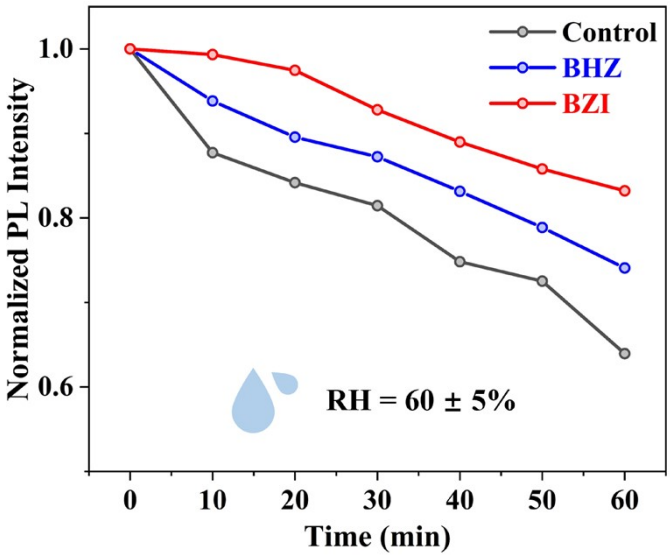

Figure S14. Normalized PL spectra of control, BHZ- and BZI-based PQDs. 40 μL of MeOAc was introduced into 1.5 mL of control, BHZ- and BZI-based PQD solutions, which were stored at ambient conditions with a relative humidity of 60 ± 5%.

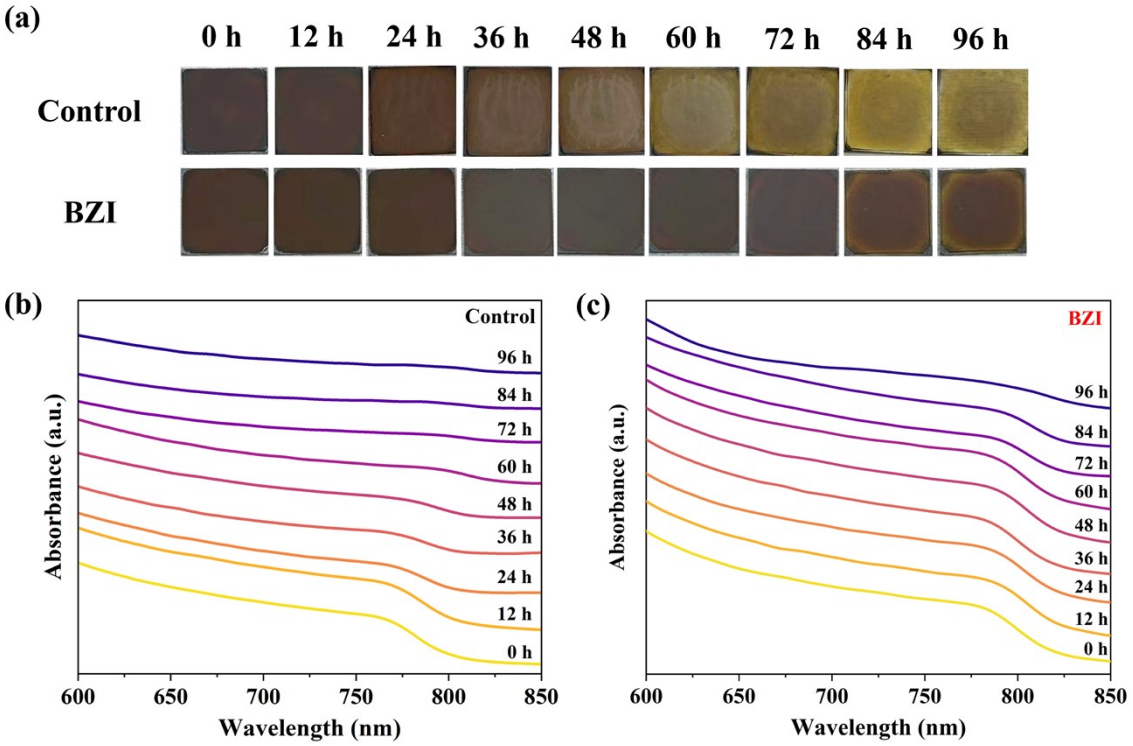

Figure S15. Thermal stability of control and BZI-based PQD solid films. (a) Photographs of control and BZI-based PQD solid films with heating. Light absorption spectra of (b) control and (c) BZI-based PQD solid films. The films were placed on a hot plate at 60°C under ambient conditions with a relative humidity of 60 ± 5%.

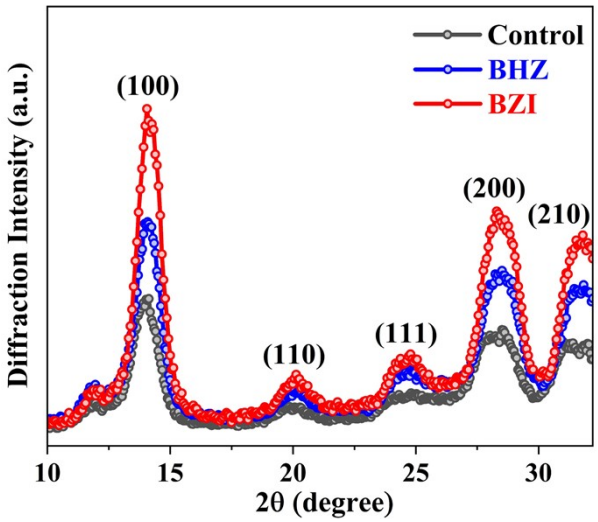

Figure S16. Radially 1D integrated profiles of the GIWAXS patterns of control, BHZ-, and BZI-based PQD solid films.

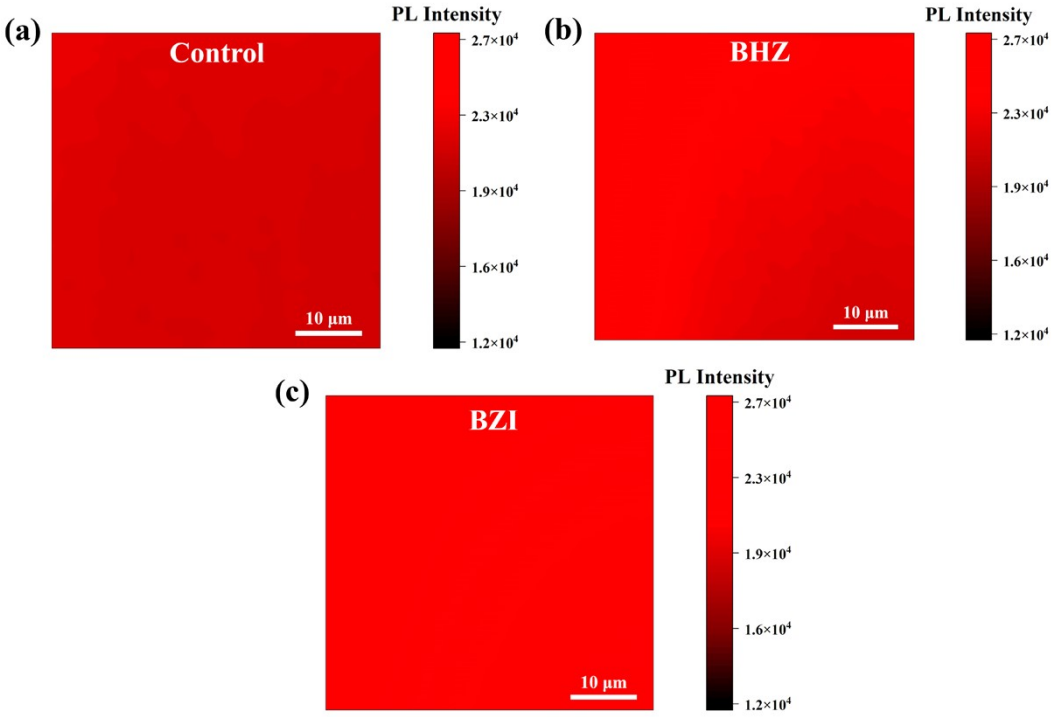

Figure S17. 2D PL mapping images of (a) control, (b) BHZ-, and (c) BZI-based PQD solid films.

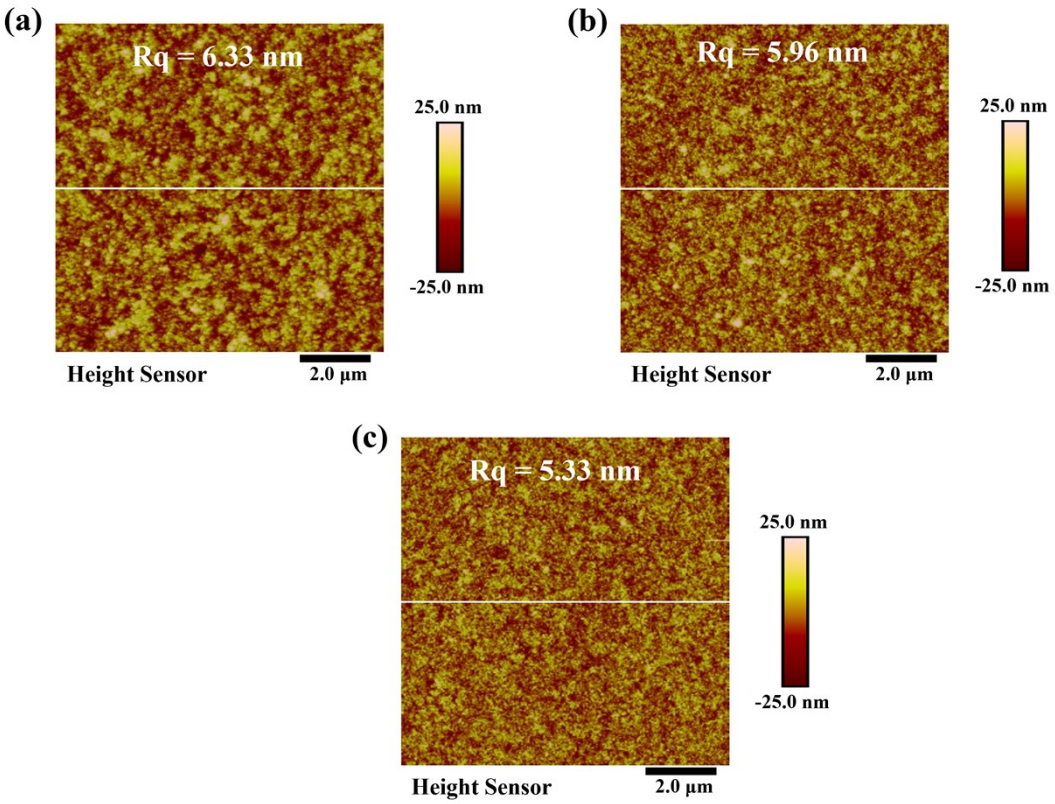

Figure S18. 2D AFM images of (a) control, (b) BHZ-, and (c) BZI-based PQD solid films.

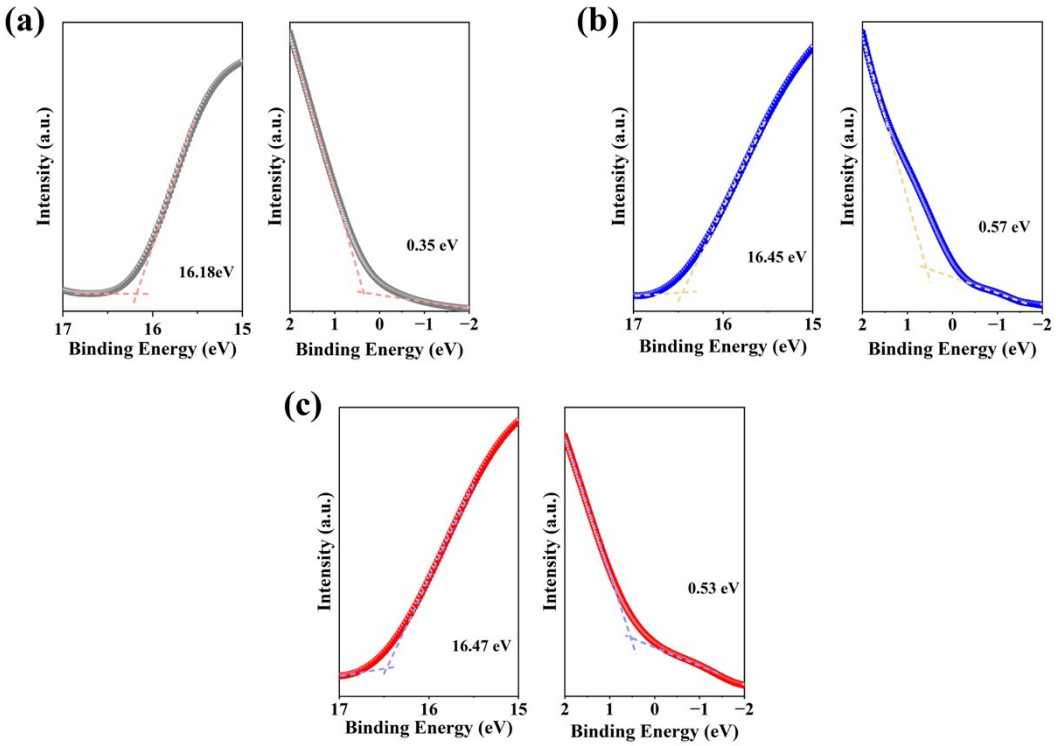

Figure S19. UPS spectra of (a) control, (b) BHZ-, and (c) BZI-based PQDs. The left panel shows the secondary electron cut-off region, and the right panel shows the valence band region.

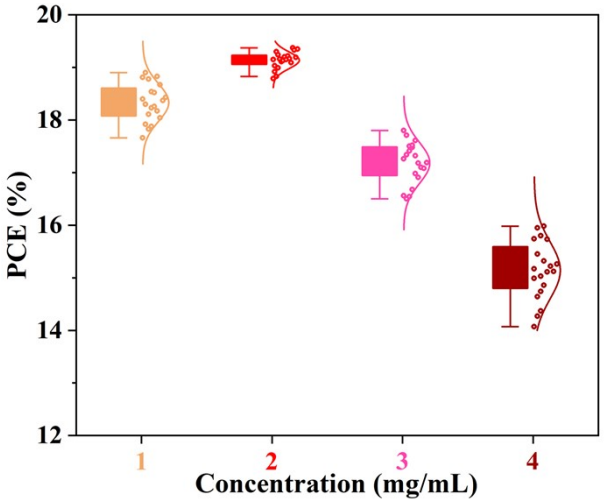

Figure S20. Statistical PCEs of the BZI-based PQDSCs fabricated using different concentrations of BZI ligands for the ISMS treatment.

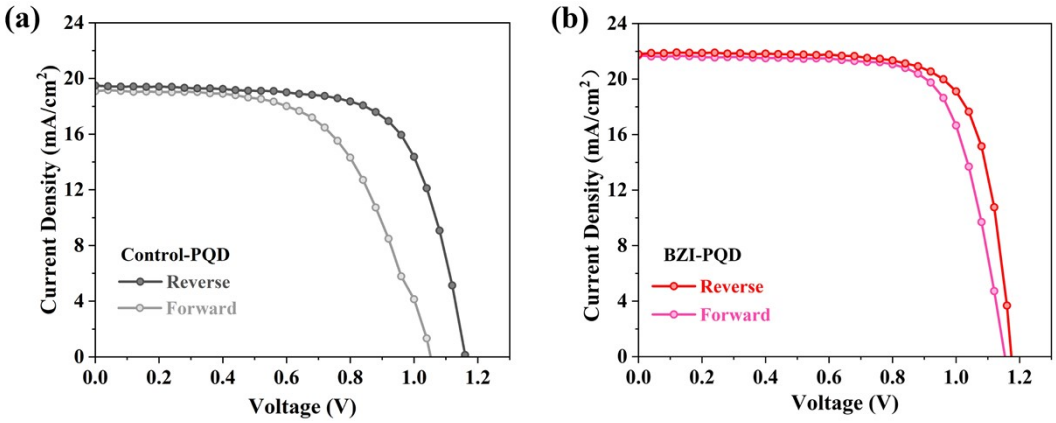

Figure S21. *J-V* curves of (a) the control and (b) BZI-based PQDSCs measured with reverse (from V_{OC} to J_{SC}) and forward (from J_{SC} to V_{OC}) voltage scanning directions.

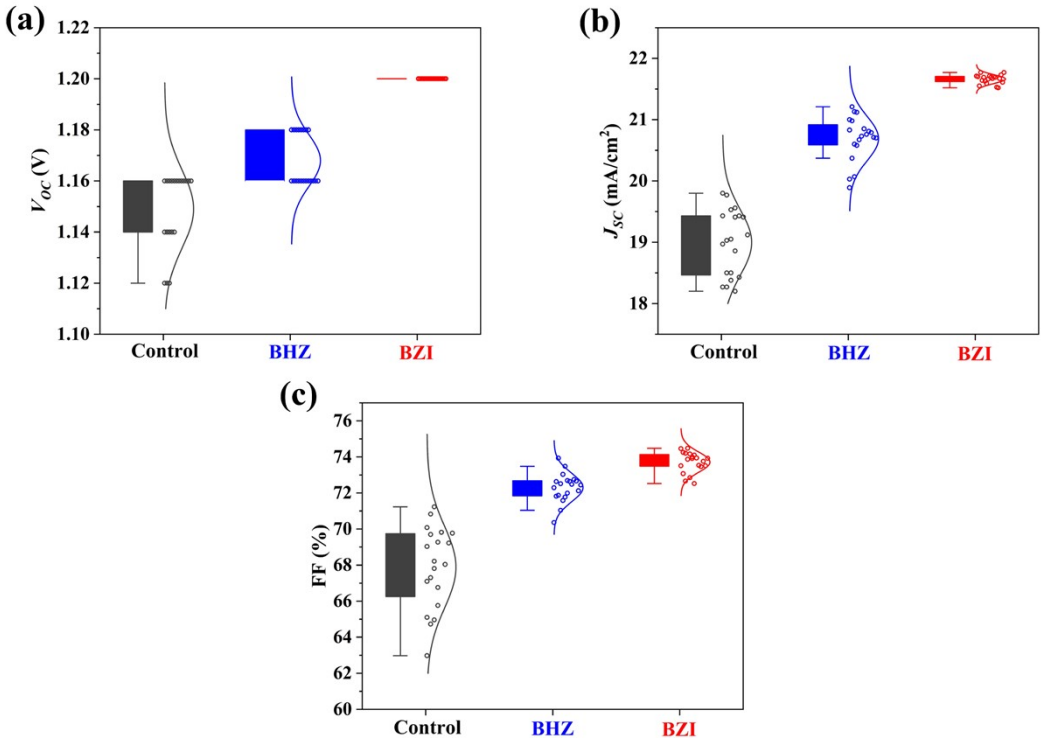

Figure S22. Statistical (a) V_{OC}, (b) J_{SC}, and (c) FF of control, BHZ- and BZI-based PQDSCs. 20 devices fabricated from different batches were applied for statistics.

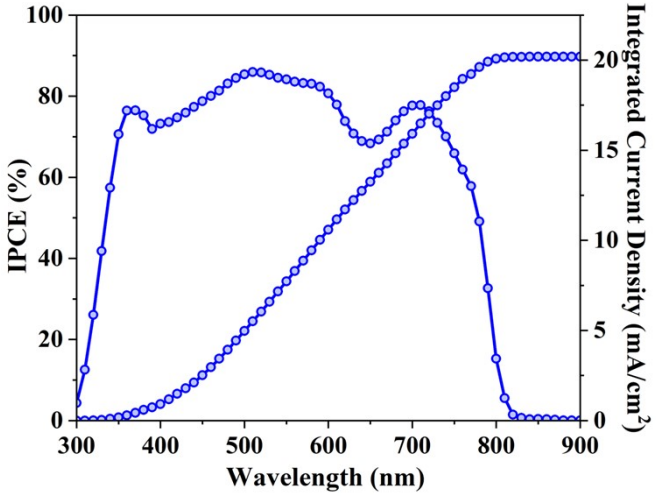

Figure S23. IPCE spectrum of the BHZ-based PQDSC.

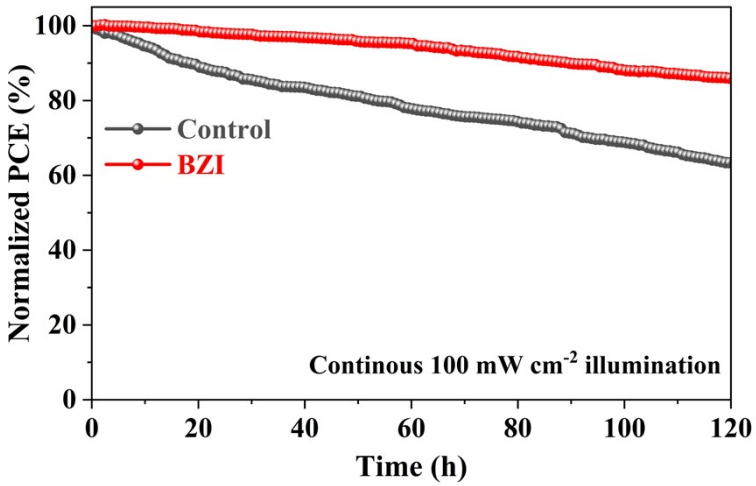

Figure S24. Photostability of unencapsulated control and BZI-based PQDSCs under continuous 100 mW/cm^2 illumination. BZI-based PQDSC retains ~86% of its initial PCE after 120 h, whereas the control PQDSC only remained ~63% of its initial PCE.

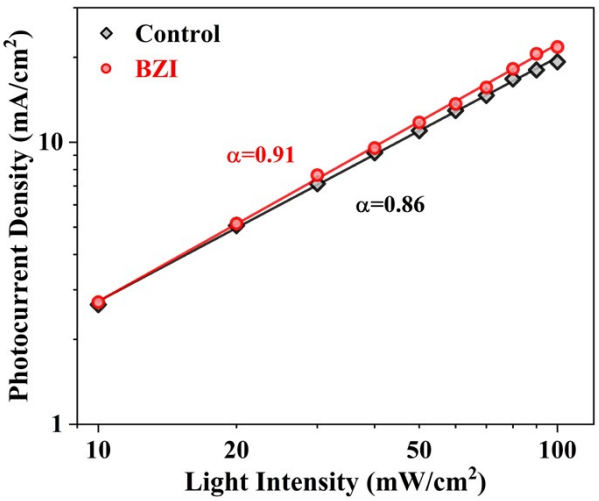

Figure S25. Light intensity-dependent J_{SC} plots of control and BZI-based PQDSCs.

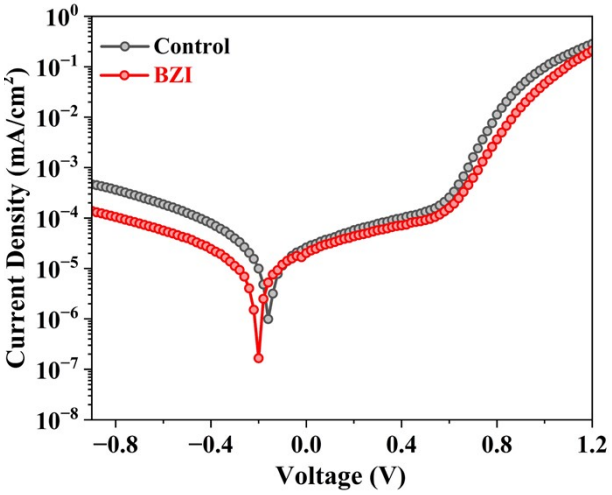

Figure S26. Dark current curves of control and BZI-based PQDSCs.

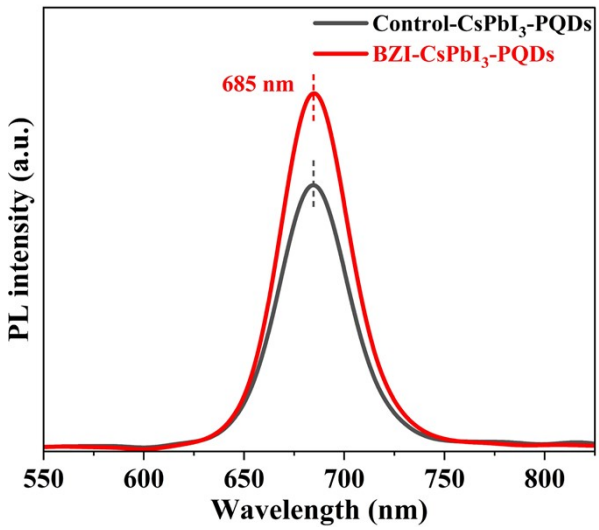

Figure S27. Steady-state PL spectra of control and BZI-based $CsPbI_3$ PQDs.

3. Supplementary Tables

Table S1. Fitted parameters of TRPL spectra of control, BHZ- and BZI-based PQDs.

PQDs	A_1	τ_1 (ns)	A_2	τ_2 (ns)	τ_{ave} (ns)
Control	0.68	5.27	0.32	23.08	17.26
BHZ	0.67	5.79	0.34	27.61	21.23
BZI	0.64	7.45	0.33	37.68	29.30

The PL decay curves were fitted by the following equation,[4]

$$I(t) = A_1 \cdot \exp\left(-\frac{t}{\tau_1}\right) + A_2 \cdot \exp\left(-\frac{t}{\tau_2}\right) + A_0 \quad \text{(Equation S1)}$$

where A_0, A_1 and A_2 are constants, t is PL decay time, τ_1 and τ_2 are fitted lifetimes. The average lifetime (τ_{ave}) is calculated using the following equation,

$$\tau_{ave} = \frac{A_1\tau_1^2 + A_2\tau_2^2}{A_1\tau_1 + A_2\tau_2} \quad \text{(Equation S2)}$$

Table S2. Summarized photovoltaic parameters of efficient $FAPbI_3$ PQDSCs.

Year	Device structure	V_{OC} (V)	J_{SC} (mA/cm^2)	FF	PCE (%)	Ref.
2018	ITO/SnO_2/$FAPbI_3$ PQDs/Spiro-OMeTAD/Au	1.10	11.83	0.64	8.38	5
2019	FTO/TiO_2/$FAPbI_3$ PQDs/Spiro-OMeTAD /MoO_x/Al	1.15	14.99	0.66	11.43	6
2020	FTO/TiO_2/ $FAPbI_3$ PQDs /polymer/PTAA/MoO_x/Ag	1.12	16.7	0.71	13.2	7
2022	ITO/PEDOT: PSS/$FAPbI_3$ PQDs /PCBM/BCP/Ag	0.89	14.56	0.78	10.13	8
2022	ITO/SnO_2/$FAPbI_3$ PQDs/Spiro-OMeTAD/Au	1.12	18.50	0.67	13.8	9
2023	FTO/TiO_2/$FAPbI_3$ PQDs/PTAA/MoO_x/Ag	1.15	18.45	0.68	14.47	10
2023	FTO/TiO_2/$FAPbI_3$ PQDs/PTAA/MoO_x/Ag	1.14	17.3	0.76	15.1	11
2023	ITO/SnO_2/$FAPbI_3$ PQDs/Spiro-OMeTAD/Au	1.15	18.03	0.73	15.34	12
2023	ITO/SnO_2/$FAPbI_3$ PQDs/Spiro-OMeTAD/Ag	1.17	19.30	0.72	16.23	13
2024	ITO/SnO_2/$FAPbI_3$ PQDs/Spiro-OMeTAD/Ag	1.16	20.95	0.67	16.29	14
2024	ITO/ZnO/SnO_2/PQD/Spiro-OMeTAD/Au	1.14	20.89	0.76	18.1	15
2024	ITO/SnO_2/$FAPbI_3$ PQDs/Spiro-OMeTAD /MoO_x/Al	1.17	17.98	0.74	15.56	16
2024	FTO/TiO_2/$FAPbI_3$ PQDs/PTAA/MoO_x/Ag	1.14	19.61	0.74	16.61	17
2024	ITO/SnO_2/$FAPbI_3$ PQDs/Spiro-OMeTAD /MoO_x/Ag	1.20	21.19	0.67	17.06	1
2025	FTO/TiO_2/$FAPbI_3$ PQDs/PTAA/MoO_x/Ag	1.11	20.85	0.72	16.68	18
2025	FTO/TiO_2/$FAPbI_3$ PQDs/PTAA/MoO_x/Ag	1.15	20.57	0.77	18.21	19
2025	FTO/TiO_2/$FAPbI_3$ PQDs/PTAA/MoO_x/Ag	1.17	21.09	0.77	19.01	20
2025	ITO/SnO_2/$FAPbI_3$ PQDs/Spiro-OMeTAD /MoO_x/Ag	1.16	21.18	0.78	19.14	21
2025	**ITO/SnO_2/$FAPbI_3$ PQDs/Spiro-OMeTAD /MoO_x/Ag**	**1.20**	**21.67**	**0.74**	**19.37**	**This work**

Table S3. Fitted parameters of TPV curves of control and BZI PQDSCs.

PQDSCs	A_1	τ_1 (ms)	A_2	τ_2 (ms)	τ_{ave} (ms)
Control	0.48	0.06	0.41	3.43	3.36
BZI	0.38	0.09	0.57	5.37	5.31

The V_{OC} decay curves were fitted by the following equation,[22]

$$V_{OC} = A_1 \cdot \exp\left(-\frac{t}{\tau_1}\right) + A_2 \cdot \exp\left(-\frac{t}{\tau_2}\right) + A_0 \quad \text{(Equation S3)}$$

where A_0, A_1 and A_2 are constants, t is V_{OC} decay time, τ_1 and τ_2 are fitted lifetimes. The average lifetime (τ_{ave}) is calculated using the following equation,

$$\tau_{ave} = \frac{A_1\tau_1^2 + A_2\tau_2^2}{A_1\tau_1 + A_2\tau_2} \quad \text{(Equation S4)}$$

Table S4. Fitted parameters of TPC curves of control and BZI PQDSCs.

PQDSCs	A_1	τ (μs)
Control	0.93	4.24
BZI	0.97	3.69

The J_{SC} decay curves were fitted using the following equation,[4]

$$J_{SC} = A_1 \cdot \exp\left(-\frac{t}{\tau}\right) + A_0 \qquad \text{(Equation S5)}$$

where A_0 and A_1 are constants, t is the J_{SC} decay time, and τ is the fitted lifetime.

4. Supplementary Notes

Note S1. Calibration of light absorption of I^-, I_2, I_3^- and BHZ.

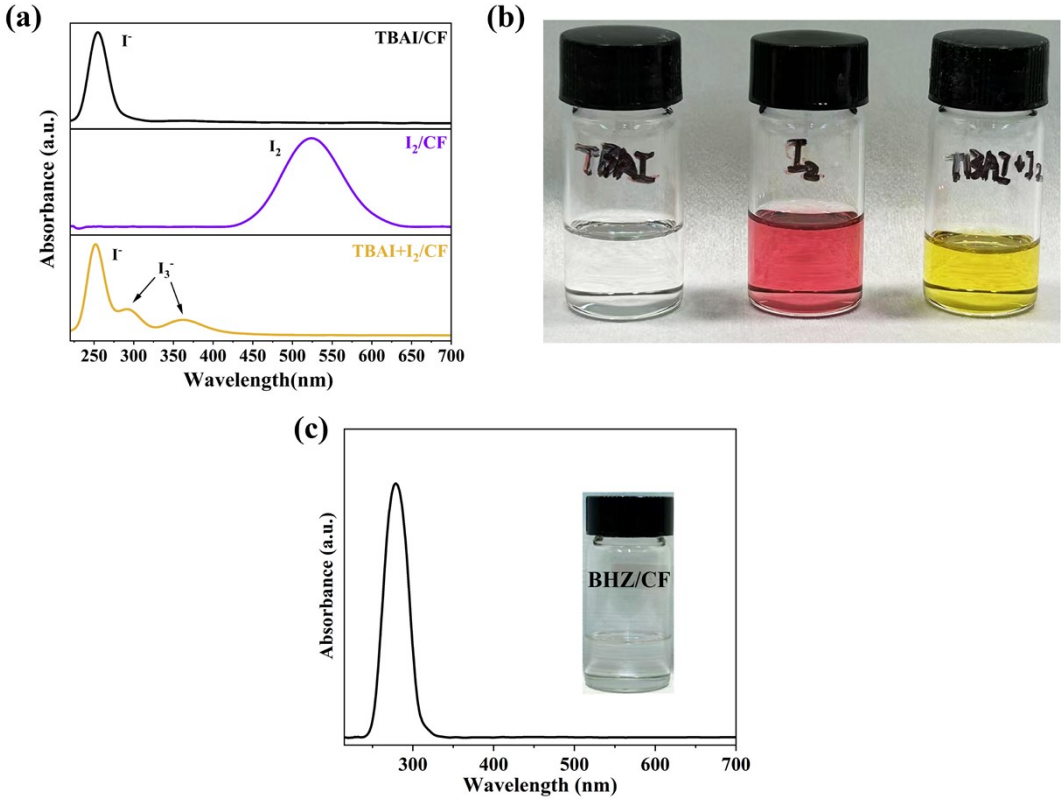

Figure S28. (a) Light absorption spectra of iodide species in chloroform (CF). Tetrabutylammonium iodide (TBAI) was employed as I^- donor (0.01 mol/L in chloroform), and iodine (I_2) was dissolved in chloroform at 0.005 mol/L. I_3^- ions were obtained by mixing TBAI and I_2 solutions. (b) Photograph of TBAI/CF, I_2/CF, and TBAI+I_2/CF solutions. (c) Light absorption of the BHZ molecules. The inserted shows the photograph of the BHZ in chloroform.

We first utilized tetrabutylammonium iodide (TBAI) and I_2 to calibrate absorption peak positions of iodide species in chloroform according to the literature.[23] As shown in **Figure S28a**, the absorption peaks of I^- and I_2 are located at ~254 and ~525 nm, respectively. After combining excess TBAI with I_2 in the chloroform, the solution changed color from plum to yellow (**Figure S28b)**, and the I_2 peaks disappeared, with two new peaks appearing at ~293 and ~365 nm, corresponding to the characteristic absorption peaks of I_3^- anions. Since the conjugated aromatic ring in the phenyl group also possesses absorption peaks in the near-ultraviolet region, we further measured the light absorption spectrum of the BHZ in chloroform. **Figure S28c** displays a colorless solution with a broad absorption band at ~280 nm in the light absorption spectrum, attributed to $\pi \rightarrow \pi^*$ electron transition in the phenyl group

and n→π* electron transition in the C=O group under a long-conjugated system. These calibrations provide reliable references of peak locations of I^-, I_2, I_3^- and BHZ in chloroform, enabling us to monitor the composition variations in chloroform with different molar ratios between I_2 and BHZ.

Note S2. Optoelectronic properties and stability of PEAI- and BZI-based PQDs.

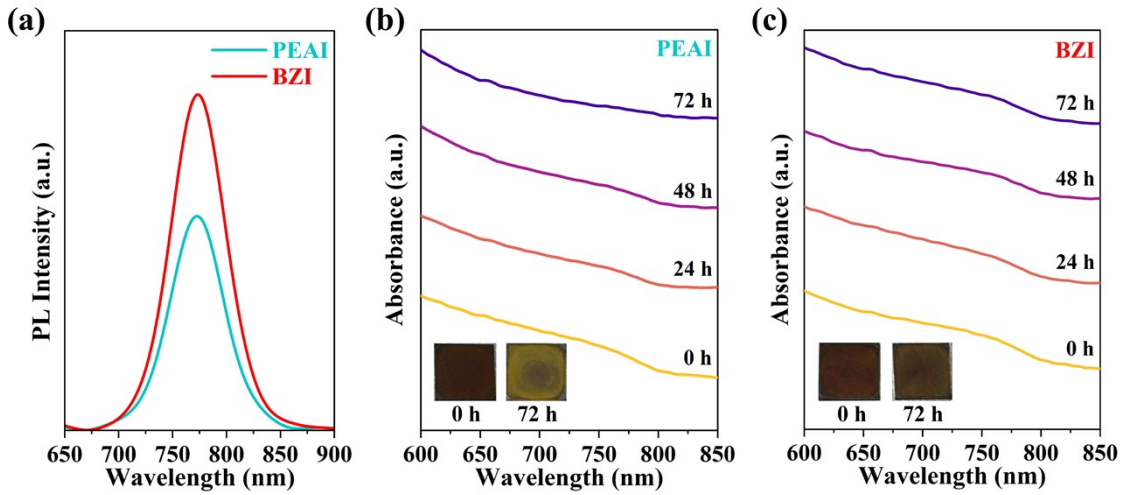

Figure S29. (a) Steady-state PL spectra of PEAI- and BZI-based PQDs. Light absorption spectra of (b) PEAI- and (c) BZI-based PQD solid films. The films were placed on a hot plate at 80℃ under ambient conditions with a relative humidity of 60 ± 5%. Insets show the photographs of the films before and after the storage.

Based on the ameliorated optoelectronic properties and environmental stabilities in BZI-based PQDs, we further investigated the strong bonding interaction of the BZI ligands on the surface matrix of PQDs. We treated the PQDs with conventional 2-phenylethylamine hydroiodide (PEAI) in acetonitrile during the purification of PQDs to obtain PEAI-based PQDs. The PEA^+ has a similar molecular structure to the BZ^+, but BZ^+ possesses an additional carbonyl group (C=O). **Figure S29a** displays the steady-state PL spectra of PEAI- and BZI-based PQDs, and the higher PL intensity of BZI-based PQDs indicates that the carbonyl group of BZ^+ could bind strongly to the uncoordinated Pb^{2+} cations to effectively inhibit nonradiative recombination induced by the trap states. Moreover, we also conducted thermal stability for these PQD solid films on a hot plate at 80 ℃ under ambient conditions with a relative humidity of 60 ± 5%. As illustrated in **Figure S29b**, the light absorption band edge of PEAI-based PQD film reduced after continuous heating for 72 h, and the photograph shows the film turned into the yellow phase, which may be attributed to the desorption of PEA^+ ions from the PQD surface under continuous heating. Instead, the light absorption band edge of the BZI-based PQD film remained stable after 72 h, and the film was still black (**Figure S29c**), which demonstrates that BZ^+ could anchor stably on the surface matrix of PQDs due to the strong bonding interactions of the C=O to the uncoordinated Pb^{2+} cations on the surface matrix of PQDs.

5. Supplementary References

1. M. Zhang, X. Mei, G. Wang, J. Qiu, Z. Sun and X. Zhang, *Energy Environ. Sci.*, 2024, **18**, 300-312.
2. D. Jia, J. Chen, R. Zhuang, Y. Hua and X. Zhang, *Adv. Mater.*, 2023, **35**, 2212160.
3. D. Jia, J. Chen, X. Mei, W. Fan, S. Luo, M. Yu, J. Liu and X. Zhang, *Energy Environ. Sci.*, 2021, **14**, 4599-4609.
4. Q. Zhou, J. Qiu, Y. Wang, M. Yu, J. Liu and X. Zhang, *ACS Energy Lett.*, 2021, **6**, 1596-1606.
5. J. Xue, J.-W. Lee, Z. Dai, R. Wang, S. Nuryyeva, M. E. Liao, S.-Y. Chang, L. Meng, D. Meng, P. Sun, O. Lin, M. S. Goorsky and Y. Yang, *Joule*, 2018, **2**, 1866-1878.
6. Q. Zhao, A. Hazarika, X. Chen, S. P. Harvey, B. W. Larson, G. R. Teeter, J. Liu, T. Song, C. Xiao, L. Shaw, M. Zhang, G. Li, M. C. Beard and J. M. Luther, *Nat. Commun.*, 2019, **10**, 2842.
7. K. Ji, J. Yuan, F. Li, Y. Shi, X. Ling, X. Zhang, Y. Zhang, H. Lu, J. Yuan and W. Ma, *J. Mater. Chem. A*, 2020, **8**, 8104-8112.
8. Y. Xu, H. Li, S. Ramakrishnan, D. Song, Y. Zhang, M. Cotlet and Q. Yu, *ACS Appl. Energy Mater.*, 2022, **5**, 9858-9869.
9. S. Ding, M. Hao, C. Fu, T. Lin, A. Baktash, P. Chen, D. He, C. Zhang, W. Chen, A. K. Whittaker, Y. Bai and L. Wang, *Adv. Sci.*, 2022, **9**, 2204476.
10. X. Zhang, H. Huang, L. Jin, C. Wen, Q. Zhao, C. Zhao, J. Guo, C. Cheng, H. Wang, L. Zhang, Y. Li, Y. M. Maung, J. Yuan and W. Ma, *Angew. Chem. Int. Ed.*, 2023, **62**, e202214241.
11. F. Li, X. Zhang, J. Shi, L. Jin, J. Qiao, J. Guo, H. Yin, Y. Li, J. Yuan and W. Ma, *Adv. Funct. Mater.*, 2023, **33**, 2302542.
12. S. Ding, J. A. Steele, P. Chen, T. Lin, D. He, C. Zhang, X. Fan, E. Solano, A. K. Whittaker, M. Hao and L. Wang, *Adv. Energy Mater.*, 2023, **13**, 2301817.
13. M. Li, Y. Bao, W. Hui, K. Sun, L. Gu, X. Kang, D. Wang, B. Wang, H. Deng, R. Guo, Z. Li, X. Jiang, P. Müller-Buschbaum, L. Song and W. Huang, *Adv. Mater.*, 2023, **36**, 2309890.
14. M. Zhang, Q. Gao, X. Mei, J. Qiu, R. Zhuang, Y. Hua, Z. Sun and X. Zhang, *Energy Environ. Sci.*, 2024, **17**, 2145-2156.
15. H. Aqoma, S.-H. Lee, I. F. Imran, J.-H. Hwang, S.-H. Lee and S.-Y. Jang, *Nat. Energy*, 2024, **9**, 324-332.
16. S.-H. Jo, W. Yang, Y. Tang, D.-H. Kim, W. Lee, J. Park, S. E. Chang, S. Y. Lim, S. Kim, Y. S. Lee, J. Y. Kim, J. Lim, B. Hu, K. Zhu and T.-W. Lee, *ACS Energy Lett.*, 2024, **9**, 2807-2815.
17. X. Zhang, H. Huang, C. Zhao, L. Jin, C. Lee, Y. Li, D.-H. Ko, W. Ma, T. Wu and J. Yuan, *Nat. Energy*, 2024, **9**, 1378-1387.
18. X. Sun, L. Yuan, Y. Liu, G. Shi, Y. Wang, C. Liu, X. Zhang, Y. Zhao, C. Zhao, M. Ma, B. Shen, Y. Wang, Q. Shen, Z. Liu and W. Ma, *Nat. Synth.*, 2025, **4**, 167-176.
19. D. Li, C. Zhao, X. Zhang, X. Zhao, H. Huang, H. Li, F. Li and J. Yuan, *Adv. Mater.*, 2025, **37**, 2417346.
20. C. Zhao, D. Li, X. Zhang, H. Huang, C. Cazorla, X. Zhao, H. Li, Y. Chen, W. Zhu, T. Wu and J. Yuan, *Adv. Mater.*, 2025, e12201.
21. M. Zhang, S. Huang, X. Mei, G. Wang, B. Ren, J. Qiu, Z. Yuan and X. Zhang, *Energy Environ. Sci.*, 2025, **18**, 8964-8976.
22. D. Jia, J. Chen, S. Zheng, D. Phuyal, M. Yu, L. Tian, J. Liu, O. Karis, H. Rensmo, E. M. J. Johansson and X. Zhang, *Adv. Energy Mater.*, 2019, **9**, 1902809.
23. J. Chen, D. Jia, R. Zhuang, Y. Hua and X. Zhang, *Adv. Mater.*, 2022, **34**, 2204259.